A Shock Tube Study of OH + H_2O_2 → H_2O + HO_2 and H_2O_2 + M → 2OH + M using Laser Absorption of H_2O and OH

Zekai Hong,* Robert D. Cook, David F. Davidson, and Ronald K. Hanson

Department of Mechanical Engineering, Stanford University, Stanford, California 94305, USA

Received: January 8, 2010; Revised Manuscript Received: April 2, 2010

The rate constants of the reactions

$$H_2O_2 + M \rightarrow 2OH + M \quad (1)$$

$$OH + H_2O_2 \rightarrow H_2O + HO_2 \quad (2)$$

were measured in shock-heated H_2O_2/Ar mixtures using laser absorption diagnostics for H_2O and OH. Time-histories of H_2O were monitored using tunable diode laser absorption at 2550.96 nm, and time-histories of OH were achieved using ring dye laser absorption at 306 nm. Initial H_2O_2 concentrations were also determined utilizing the H_2O diagnostic. On the basis of simultaneous time-history measurements of OH and H_2O, k_2 was found to be 4.6×10^{13} exp(−2630 K/*T*) [cm^3 mol^{-1} s^{-1}] over the temperature range 1020−1460 K at 1.8 atm; additional measurements of k_2 near 1 atm showed no significant pressure dependence. Similarly, k_1 was found to be 9.5×10^{15} exp(−21 250 K/*T*) [cm^3 mol^{-1} s^{-1}] over the same temperature and pressure range.

1. Introduction

Hydrocarbon ignition at intermediate temperatures (850−1200 K) is controlled by hydrogen peroxide (H_2O_2) and hydroperoxyl radical (HO_2) reactions. These reactions are regarded as "the central kinetic feature in engine knock in spark ignition engines, in ignition in liquid-fueled diesel engines, and in the operation of homogeneous charge, compression ignition (HCCI) engines."[1] The H_2O_2 thermal decomposition system provides a unique opportunity to isolate and study H_2O_2 and HO_2 reactions at combustion temperatures.

For example, a reliable, clean HO_2 precursor is desirable to study HO_2 reactions with alkyl radicals. The H_2O_2 decomposition system is a possible way to fulfill this need, since HO_2 is produced by a simple two-step process:

$$H_2O_2 + M \rightarrow OH + OH + M \quad (1)$$

$$OH + H_2O_2 \rightarrow H_2O + HO_2 \quad (2)$$

Reaction 2 has received considerable attention near room temperature[2−12] because OH and HO_2 catalyze the destruction of ozone (O_3), and H_2O_2 is an important reservoir for both radicals. The low temperature experimental data for k_2 show good consistency, ranging from 9.3×10^{11} to 1.20×10^{12} [cm^3 mol^{-1} s^{-1}] at 298 K. However, some researchers reported a small positive temperature dependence of the rate constant[2−6,8] whereas others found a negative temperature dependence[7,9] over their measured temperature ranges. Atkinson et al.[12] reviewed the available low temperature data and proposed an evaluated rate expression of $k_2 = 1.75 \times 10^{12}$ exp(−160 K/*T*) [cm^3 mol^{-1} s^{-1}] with a value of 1.02×10^{12} at room temperature.

As opposed to the extensive studies at low temperatures, only two studies of reaction 2[13−15] were conducted at combustion temperatures, and these were both performed in the same laboratory. The limited availability of experimental data for k_2 is due to the unstable nature of H_2O_2 at high temperatures and the lack of sensitive diagnostics for H_2O_2. The earlier study[13] essentially inferred the ratio of the rates for the two reactions, OH + H_2O_2 → H_2O + HO_2 and OH + HO_2 → H_2O + O_2. The expression for k_2 from the most recent Hippler et al. study[14] is widely used in chemical kinetics models for combustion[16−19] and accepted in the latest evaluation by Baulch et al.[20] An unusual up-turn in the reaction rate at temperatures higher than 800 K was reported by Hippler et al.[14]

Recently, a new systematic approach for studying the thermal decomposition of H_2O_2 at combustion temperatures was reported.[21] In light of this newly developed method, better-controlled experiments can be designed to study other major reactions within the H_2O_2 decomposition system. Here we report our latest work on the reaction OH + H_2O_2 → H_2O + HO_2 and extend our previous measurements of H_2O_2 + M → 2OH + M to higher temperatures, both with additional measurements of OH using ring dye laser absorption in the ultraviolet.

2. Experimental Setup

2.1. Shock Tube with Modified Driver Section. The experiments were carried out in a high-purity, 304 stainless steel shock tube with inner diameter of 14.1 cm. The driven section of the shock tube is 8.5 m long, and the driver section is 3.3 m long. Conditions behind reflected shocks were determined using normal-shock relations. Incident-shock velocity measurements

* To whom correspondence should be addressed.

10.1021/jp100204z
Published on Web 04/16/2010

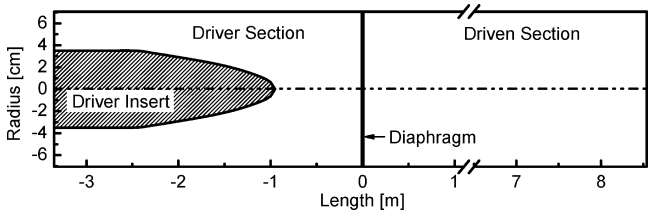

Figure 1. Scale drawing of the driver-insert configuration. After the diaphragm rupture, the incident shock wave propagates from left to right, and an expansion wave propagates from right to left.

were made using five piezoelectric pressure transducers (PCB) over the last 1.5 m of the shock tube, allowing accurate extrapolation to infer the incident shock velocity at the endwall. Uncertainty in the initial temperature behind the reflected shock wave, T_5, was ±0.8%.[22] In addition to the five PCB pressure transducers for incident-shock velocity measurements, another sidewall piezoelectric pressure transducer (Kistler model 603B) located 2 cm from the endwall was used to monitor pressure time-histories.

Accurate rate measurements in reflected shock wave experiments rely on the near-constant-volume performance of large-diameter shock tubes at short test times (less than 1−2 ms). At longer test times, small increases in temperature and pressure in the reflected shock conditions can occur due to facility-related nonideal effects, such as boundary layer growth and shock attenuation. These nonideal effects can be compensated for by using driver inserts. The design of the driver insert was based on a recently developed semianalytical model.[23] A scale drawing of the primary insert configuration used in the current work is shown in Figure 1. We have demonstrated that by using the driver insert method, we can successfully maintain a highly uniform pressure and temperature profile for up to 8 ms behind the reflected shock. These small variations in temperature have been confirmed by in situ temperature measurements.[23,24] In the current study, postshock pressure fluctuations for all the shocks are less than ±2%, and the corresponding long-time temperature uncertainty is evaluated to be less than ±0.8%.

2.2. Tunable Diode Laser Absorption of H_2O near 2.55 μm. The H_2O concentration time-histories were measured 2 cm from the end wall of the shock tube using laser absorption of H_2O at 2550.96 nm (3920.09 cm^{-1}) within the υ_3 fundamental vibrational band. Almost all spectral parameters for this transition were taken from HITRAN.[25] The collisional-broadening coefficient (half-width at half-maximum per atm) for argon (not available in HITRAN) was measured in the shock tube over a temperature range between 1000 and 1600 K by matching the peak of the fitted Voigt profile to the measured line center absorbance of a known amount of H_2O and was found to be $\gamma_{Ar}(T) = 0.0277(296/T)^{0.50}$ [cm^{-1} atm^{-1}]. Details of this H_2O absorption diagnostic can be found in the literature.[21]

A distributed feedback (DFB) diode laser near 2.55 μm from Nanoplus GmbH was used. Shortly before taking data, the laser was scanned over the water line to ensure it was located at the line center. The laser beam was collimated by a lens, transmitted through the shock tube and a JDSU narrow-bandpass filter (JDSU N02548−8, center wavelength: 2546 nm, half width: 46 nm), focused by a short-focal-length convex lens into an integrating sphere (SphereOptics SPH-1G-3) to reduce beam-steering effects, and detected by a liquid nitrogen-cooled InSb detector (IR Associates IS-2.0, 1 MHz bandwidth). The horizontal laser beam crosses the axis of the shock tube so that the path length of the measurement is the inner diameter of the shock tube. The beam path outside the shock tube was purged with pure N_2 to minimize laser attenuation from ambient H_2O.

2.3. Ring-Dye Laser Absorption of OH near 306.7 nm. The laser beam path for the OH absorption diagnostic was in the same axial plane (but rotated by 45°) as the H_2O diagnostic (2 cm from the shock tube endwall), allowing for simultaneous measurement of OH and H_2O time-histories. A pair of fused-silica windows was installed on the shock tube sidewalls to allow the transmission of the OH laser.

The $R_1(5)$ line of the OH $A^2\Sigma^+-X^2\Pi$ (0,0) band near 306.7 nm, chosen for the current study, has been well-characterized and extensively utilized in chemical kinetics studies in the past.[22,26,27] The absorption coefficient of the OH radical is well-established, and measured OH concentrations are accurate to better than ±5%.[22]

To generate 306.7 nm light, a 5 W, 532 nm, cw beam produced by a Coherent Verdi laser pumps a Spectra-Physics 380 ring-dye laser operating with Rhodamine R6G dye was used to generate visible light at 613.4 nm. UV light (1−2 mW) at 306.7 nm was generated by intracavity frequency doubling using a temperature-tuned AD*A crystal. Wavelength was determined using a Burleigh WA-1000 wavemeter, and mode quality of the visible light was examined by a scanning interferometer.

A part of the UV beam was split off as the reference beam; the remaining part was transmitted through the shock tube for OH absorption. Both the reference and the transmitted beams were monitored by Thorlabs PDA 36A detectors modified with large area Hamamatsu S1722−02 photo diodes (with an effective active area of 13.2 mm^2). Both detectors were shielded by two identical spectral filters (Newport FSR-UG11, center wavelength: 340 nm, half width: 70 nm) to reduce broadband interference. Further details of the OH ring-dye laser absorption diagnostic may be found in Herbon et al.[22]

2.4. H_2O_2 Source. Urea−H_2O_2 (carbamide peroxide, formula: $(NH_2)_2CO{\bullet}H_2O_2$) has proven to be a reliable laboratory source of H_2O_2 vapor.[21,28] Approximately 10 g of urea−hydrogen peroxide powder (Sigma-Aldrich, 15−17% active oxygen basis) was mixed with roughly an equivalent amount of sand (SiO_2, Sigma-Aldrich) in a polycarbonate flask to prevent agglomeration. The flask was sealed with a platinum-cured silicone stopper and placed in a water bath. Upon gentle heating (48 °C), urea−H_2O_2 powder decomposes to yield H_2O_2 vapor and urea solid. The H_2O_2 formed was carried into the shock tube test section by a stream of research grade argon (99.999%) that was passed through the flask at a flow rate of 0.4−0.5 SLPM (standard liters per minute) to obtain a typical H_2O_2 concentration of about 1500 ppm. A stable supply of H_2O_2 at this rate can be generated for approximately 3−4 h. The H_2O_2/carrier gas mixture was then directed into the driven section of the shock tube from a filling port near the endwall.

Previous work[21] has found that H_2O_2 decomposes inside the shock tube on time scales of the order of 15 min, and this decomposition has been attributed to the heterogeneous reaction of H_2O_2 on the shock tube wall surfaces. To minimize the contact time between H_2O_2 vapor and the shock tube walls, a stratified filling technique has been developed.[21] The shock tube was first filled with H_2O_2/argon mixture to about 10−14 Torr (3−4 min); then the shock tube was raised to the target preshock pressure P_1 with pure argon using a filling port near the diaphragm location, thereby compressing the initial H_2O_2 mixture into a smaller volume in the test section adjacent to the endwall.

3. Analysis

3.1. Overview of Approach. Four reactions dominate the thermal decomposition of H_2O_2. The two reactions mentioned

in the introduction section yield OH and HO_2 radicals, and two others consume the radicals:

$$OH + HO_2 \rightarrow H_2O + O_2 \quad (3)$$

$$HO_2 + HO_2 \rightarrow H_2O_2 + O_2 \quad (4)$$

OH radicals are primarily formed by reaction 1 and removed by reactions 2 and 3. Therefore, the time evolution of OH can be described by:

$$\frac{d[OH]}{dt} = 2k_1[H_2O_2][M] - k_2[OH][H_2O_2] - k_3[OH][HO_2] \quad (1)$$

OH initially builds up following the decomposition of H_2O_2 and is gradually depleted due to reactions 2 and 3. When OH concentration peaks, the above equation can be rewritten as:

$$k_2 = 2k_1\frac{[M]}{[OH]_{peak}} - k_3\frac{[HO_2]}{[H_2O_2]} \quad (3)$$

Considering that reaction 2 is the major HO_2 formation channel, only a small amount of HO_2 is present when the OH concentration is at its peak. Therefore, the second term on the right can be dropped, and to first order, the rate constant of the title reaction can be related to k_1 and $[OH]_{peak}$ by:

$$k_2 \approx 2k_1\frac{[M]}{[OH]_{peak}} \quad (4a)$$

3.2. Analysis Using Detailed Kinetics Model. Data analysis and simulations were performed using an updated version of the chemical kinetics mechanism, GRI-Mech 3.0.[16] The mechanism has been updated to incorporate the latest data for the OH heat of formation,[22,30] the HO_2 heat of formation,[31] the rate constant for the reaction $OH + HO_2 \rightarrow H_2O + O_2$ ($k_3 = 4.28 \times 10^{13}$ $(T/300)^{-0.21}$ $\exp(113/T)$ [cm^3 mol^{-1} s^{-1}]),[32] and the thermal decomposition rate of H_2O_2.[21] Using this mechanism, a sensitivity analysis[21] for OH was performed with the Senkin[29] kinetics code package. The results of the sensitivity analysis coincide with our expectation that two reactions control the time evolution of OH: $H_2O_2 + M \rightarrow 2OH + M$, which shows predominantly positive sensitivity, and $OH + H_2O_2 \rightarrow H_2O + HO_2$, which shows predominantly negative sensitivity. Sensitivity analysis plots are presented later in the paper.

As will become evident from these sensitivity analyses, the kinetics that control OH and H_2O formation in the H_2O_2 thermal decomposition system can be well-described by a small set of reactions, which consists of two major reactions, 1 and 2, and three minor reactions, 3−5. Reactions 1−4 have been mentioned earlier in the paper, and reaction 5 is:

$$OH + OH \rightarrow H_2O + O \quad (5)$$

The limited number of reaction rate constants that do show a significant effect on the modeling of the experimental measurements are called active parameters.[33,34] Of the five identified active parameters, the rate constants of reactions 1, 2, and 5 will be determined experimentally in the current study. The coefficient for reaction 3 is updated from our recent study,[32] and the rate constant expression for reaction 4 is that used in almost all other recent mechanisms[17−19] and is based on the Kappel et al. study.[15]

Because of the limited number of important reaction rate constants, the results of this study are nearly immune to the choice of the base kinetic mechanism. With this expectation, we tested two representative mechanisms, the modified GRI-Mech 3.0 as previously described and the Li et al. model.[18] If identical k_1 and k_2 expressions are used, the two mechanisms predict effectively indistinguishable H_2O time-histories and near-identical OH time-histories. The small difference in the predicted OH concentrations stems from the different rate expressions used for k_5, as GRI-Mech 3.0 uses Wooldridge et al.[35] data and the Li et al. model[18] uses results from the work by Sutherland et al.[36] However, this small difference does not affect our determination of k_1 and k_2, as will become evident in Section 4. In this study, we use the modified GRI-Mech 3.0 as the base kinetic model.

3.3. Test Mixture Nonuniformity Considerations. It is possible that the stratified filling procedure used may introduce some axial nonuniformity in the test mixtures, but this should not affect incident shock speed. As mentioned above, we have used the in situ H_2O diagnostic described in ref 21 to accurately determine the mixture composition at the test location. Because extremely diluted test mixtures were used in this study, small axial variations in mixture composition will have very small influence on the incident shock speed and reflected shock temperatures. Comparisons between the 4000 ppm H_2O_2/H_2O mixtures used in this study and pure Ar shock wave experiments indicate that at most, a maximum of only 6 K difference may be expected in reflected shock temperatures.

It may be possible that radial H_2O_2 concentration gradients could exist if H_2O_2 undergoes significant surface decomposition on the sidewall of the shock tube. However, although some reaction of H_2O_2 may occur at the shock tube wall, such effects are limited by the slow H_2O_2 diffusion rate to the wall. A rearrangement of eq 3 shows that the measured $[OH]_{peak}$ is not a strong function of H_2O_2 concentration, thus the k_2 rate coefficient determination is also not a strong function of H_2O_2 concentration or its varying radial distribution. In fact, simulations using variable amounts of H_2O_2 have indicated that the entire OH profile is not a strong function of the initial H_2O_2 concentration.

4. Results and Discussion

4.1. Lower Temperature (1000 < *T* < 1200 K) Example Case. It has been demonstrated in the study by Hong et al.[21] that in the temperature range from 1000 to 1200 K, H_2O formation during the decomposition of H_2O_2 is predominantly controlled by k_1. No other reaction shows significant sensitivity at temperatures ranging from 1000 to 1200 K.[21]

From the analysis in Section 3, it is natural to select the OH diagnostic for the determination of k_2. We chose to also implement the simultaneous H_2O diagnostic for two reasons: (1) with initial H_2O_2 concentrations measured using the H_2O diagnostic,[21] comprehensive kinetics analyses can be performed for OH time-histories; and (2) with real-time k_1 determinations using the H_2O diagnostic, the temperature uncertainty in k_1 does not propagate to k_2.

Considering that the overall reaction of H_2O_2 decomposition is described by

$$H_2O_2 = H_2O + \tfrac{1}{2}O_2$$

and noting the mole-for-mole conversion between H_2O_2 and H_2O, initial H_2O_2 loadings can be inferred from H_2O concentration profiles by taking the difference between the initial and final H_2O concentrations.[21]

Figure 2 shows an example H_2O time-history obtained at 1192 K, 1.95 atm, in an argon bath gas. H_2O concentrations at time zero and in the plateau region at later times are 1364 ppm and 3580 ppm, respectively, corresponding to an initial H_2O_2 loading of 2216 ppm. Using GRI-Mech 3.0[16] with the modifications described in Section 3, water sensitivity coefficients were calculated with the Senkin[29] kinetics code package. Figure 3 is the H_2O sensitivity plot for conditions of Figure 2, with the sensitivity coefficient α defined the same as in the ref 21.

The rate constant of the reaction $H_2O_2 + M \rightarrow 2OH + M$ (k_1) was determined by changing k_1 in the chemical kinetics model to best-fit the experimental H_2O time-histories, as described in ref 21. The value of k_1 for the example case is 1.8×10^8 [cm^3 mol^{-1} s^{-1}] with an estimated fitting error of ±10%.[21] The relatively high activation energy of the reaction $H_2O_2 + M \rightarrow 2OH + M$ (42 kcal/mol[21]) renders the rate k_1 very temperature sensitive. The uncertainty in k_1 associated with the temperature uncertainty was estimated to be 21%.[21] However, when the chemical kinetics model was updated with the experimental k_1 values for the purpose of determining k_2, the temperature uncertainty in k_1 does not propagate to k_2 since both k_1 and k_2 were evaluated simultaneously and were at exactly the same temperature. Only a 10% fitting uncertainty in k_1 propagates to k_2.

With the initial H_2O_2 concentration and k_1 determined from the H_2O diagnostic, the rate of the reaction $OH + H_2O_2 \rightarrow H_2O + HO_2$ (k_2) can be derived from the OH time-history, as OH yield is predominantly controlled by the competition between k_1 and k_2. Figure 4 shows the OH concentration time-history from the same test as Figures 2 and 3. The corresponding OH sensitivity plot is presented in Figure 5. The OH sensitivity coefficients were calculated using GRI-Mech 3.0[16] with k_1 and k_2 values updated to the experimentally determined values.

By changing k_2 in the chemical kinetics model, the calculated OH profile matches measurement in the peak OH concentration, as shown in Figure 4. The associated fitting uncertainty is estimated to be ±3%. The other two reactions that the OH yield shows sensitivity to at early times are $OH + HO_2 \rightarrow H_2O + O_2$ (k_3) and $HO_2 + HO_2 \rightarrow H_2O_2 + O_2$ (k_4). HO_2 concentration is still low when OH concentration peaks. Therefore, the calculated [OH] maximum is not significantly affected by the choice of a k_3 value. Figure 6 illustrates that even a factor of 2 uncertainty in k_3 results in only a ±3% uncertainty in the inferred k_2, and this is a much larger uncertainty in k_3 than assigned (±27%) in our recent study.[32] The rate of the reaction $HO_2 + HO_2 \rightarrow H_2O_2 + O_2$ does not affect the peak OH concentration, as can be seen in Figure 6.

Uncertainties in k_2 come from various error sources, noticeably uncertainties in k_1, OH concentration, temperature, secondary reactions, and fitting procedures. As discussed previously, the uncertainty in k_1 that propagates to k_2 is estimated to be ±10%. Secondary reactions and fitting procedures introduce uncertainties of ±3 and ±5%, respectively. The OH line strength has an estimated maximum uncertainty of ±5%.[22] At the same time, a 0.02 cm^{-1} uncertainty in UV light wavelength introduces additional ±1.5% uncertainty. The combined temperature uncertainty was evaluated to be 11 K,[21] and the associated uncertainty in k_2 is estimated to be ±2%. Therefore, the overall uncertainty of the example case at 1192 K can be estimated to be ±13%.

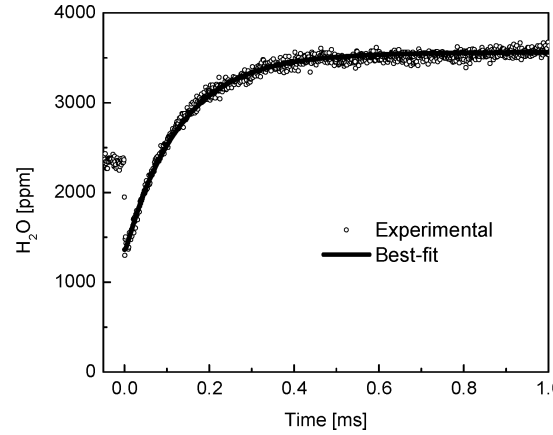

Figure 2. The dissociation rate of H_2O_2 (k_1) is fitted to be 1.8×10^8 [cm^3 mol^{-1} s^{-1}] with an estimated fitting error of ±10%. Initial test mixture: 2216 ppm H_2O_2/1364 ppm H_2O/682 ppm O_2/Ar; initial reflected shock conditions: 1.95 atm, 1192 K.

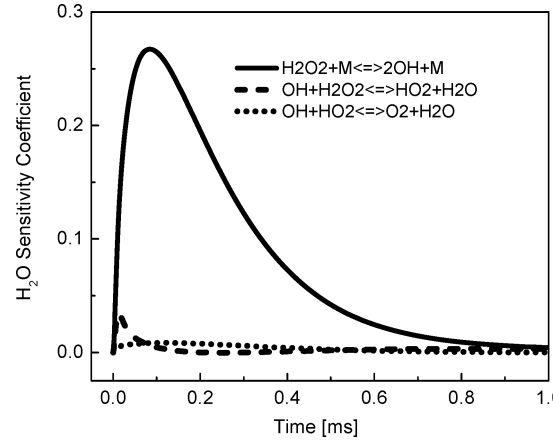

Figure 3. The formation of H_2O is predominantly controlled by the dissociation rate of H_2O_2. Conditions are those of Figure 2.

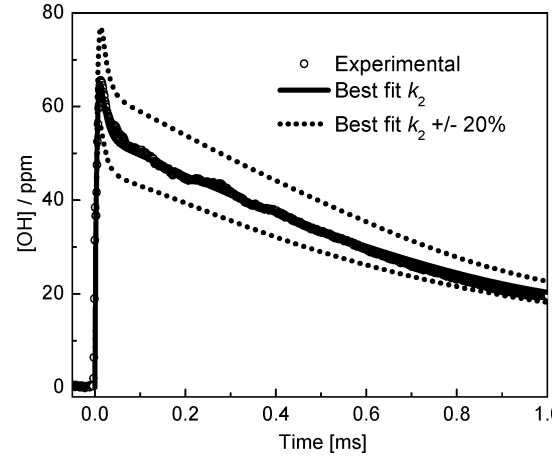

Figure 4. The rate of the reaction $OH + H_2O_2 \rightarrow H_2O + HO_2$ (k_2) is fitted to be 5.1×10^{12} [cm^3 mol^{-1} s^{-1}] with an estimated fitting error of ±3%. Special attention was paid to match the peak in OH concentration. Conditions are those of Figure 2.

It should be pointed out that OH time-histories were calculated assuming test mixtures were at constant pressure and enthalpy (constant $P-H$) behind reflected shock waves in the current study, as opposed to a usually assumed constant volume

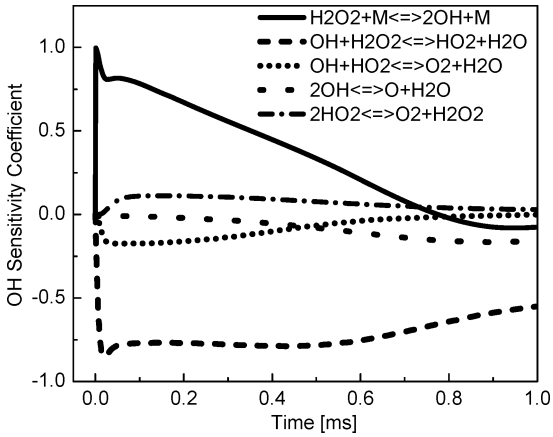

Figure 5. OH yield is predominantly controlled by the competition between the OH formation reaction $H_2O_2 + M \rightarrow 2OH + M$ (k_1) and the OH removal reaction $OH + H_2O_2 \rightarrow H_2O + HO_2$ (k_2). Conditions are those of Figure 2.

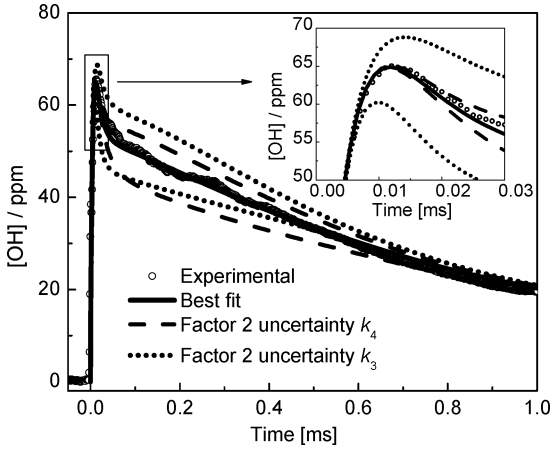

Figure 6. $[OH]_{peak}$ is controlled by k_1 and k_2. Other reactions show very minor or no impact on $[OH]_{peak}$. Conditions are those of Figure 2.

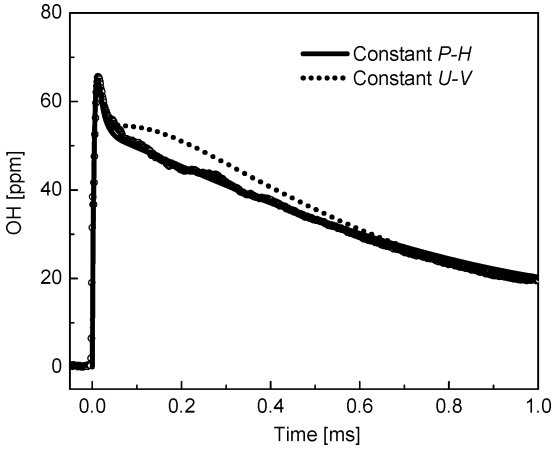

Figure 7. OH profiles predicted by assuming a constant $P-H$ process or a constant $U-V$ process behind the reflected shock wave. Identical k_1 and k_2 were used in those calculations. The two models agree on the peak OH concentration, although the constant $U-V$ model predicts a slight hump behavior after the OH spike. Conditions are those of Figure 2.

and internal energy (constant $U-V$). Shown in Figure 7 is a comparison of OH profiles calculated assuming constant $P-H$ and constant $U-V$ reactors with the identical k_1 and k_2 values. The k_1 value was determined from the H_2O time-history (Figure 2), where the two reactor models result in almost identical H_2O profiles. The k_2 value was inferred from the OH peak concentration (Figure 4), where the two models agree very well, as can been seen from the comparison in Figure 7. However, the two models start to diverge after the early time OH spike. The constant $U-V$ reactor model predicts a hump behavior, which was not observed in the experiment. No discussion on this issue was found in the work by Hippler et al.[14] as their experimental data were only compared to model calculations at early times before this discrepancy could appear.

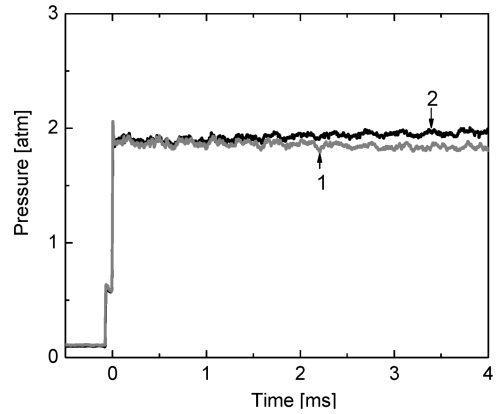

Figure 8. Comparison of pressure profiles: (1) 1134 K, 2900 ppm H_2O_2/816 ppm H_2O/Ar driven gas, with driver insert, $dP/dt = 0\%$/ms; (2) 1100 K, 2444 ppm H_2O_2/1538 ppm H_2O/Ar driven gas, without driver insert, $dP/dt = 1.3\%$/ms. All pressure profiles have been rescaled to match the initial P_5.

We initially attempted to resolve the discrepancy from a chemical kinetics perspective. The rates of the other two reactions that also show OH sensitivities, $OH + HO_2 \rightarrow H_2O + O_2$ (k_3) and $HO_2 + HO_2 \rightarrow H_2O_2 + O_2$ (k_4), were both adjusted by a factor of 2 while retaining the constant $P-H$ assumption (Figure 6). None of those adjusted OH profiles show a similar hump behavior, suggesting that the discrepancy could not be explained by chemical kinetics parameters.

It is significant that k_1 is a strong function of temperature, with an activation energy of 42.1 kcal/mol.[21] In contrast, k_2 only weakly depends on temperature with an activation energy of only 5.2 kcal/mol, as will be discussed later in the paper. Therefore, a temperature rise favors k_1 and shifts the balance toward higher OH concentrations. For an exothermic system, such as the decomposition of H_2O_2, temperature rises higher in a constant $U-V$ reactor than at constant $P-H$, which apparently explains the discrepancy between the two models. At late times (>0.6 ms in Figure 7), H_2O_2 is close to depletion and temperature effects on k_1 diminish; as a result, the OH profiles calculated with both the models converge again.

The mixtures used in this study were very dilute so that increases in temperature due to the exothermicity of H_2O_2 decomposition were minimized. For the example case discussed here, GRI-Mech 3.0[16] predicts final temperature rises of 20 and 11 K by the constant $U-V$ reactor model and the constant $P-H$ reactor model, respectively. It may be possible in the future to distinguish these two reactor models by taking advantage of a highly sensitive diagnostic recently developed for shock tube temperature measurements.[24]

To ensure that the observed departure in the experimental OH profile from the commonly adopted constant $U-V$ reactor model is not a result of using the driver insert, a test was conducted without the driver insert. Pressure profiles for these experiments are shown in Figure 8.

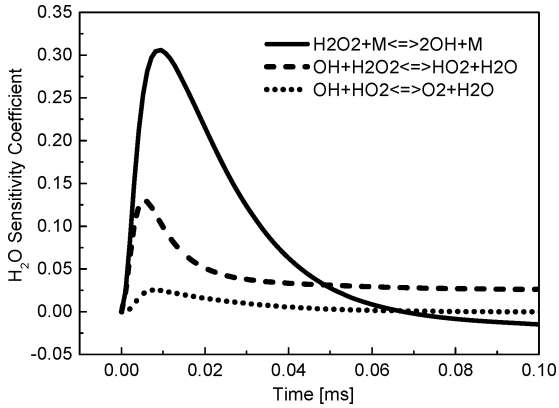

Figure 9. At higher temperatures ($T > 1200$ K), the formation of H_2O shows significant sensitivity to $OH + H_2O_2 \rightarrow H_2O + HO_2$, whereas $H_2O_2 + M \rightarrow 2OH + M$ remains the most important one. Initial test mixture: 2540 ppm H_2O_2/1234 ppm H_2O/617 ppm O_2/Ar; initial reflected shock conditions: 1.91 atm, 1398 K.

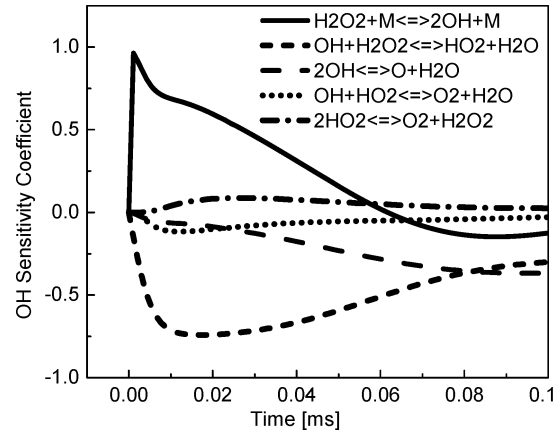

Figure 10. Similar to the example case at a lower temperature (Figure 5), OH yield at an elevated temperature is controlled by the OH formation reaction $H_2O_2 + M \rightarrow 2OH + M$ and the OH removal reaction $OH + H_2O_2 \rightarrow H_2O + HO_2$. Conditions are those of Figure 9.

Neither pressure profile in Figure 8 shows any evidence of reaction-induced pressure change, as the energy release due to chemical reaction is so small that it cannot be resolved by the pressure measurements. (The linear rise in pressure seen in profile 2 is due to facility effects such as boundary layer growth.) The measured OH time-history for the experiment without driver insert (not shown here) was very similar to the profile observed with driver insert (i.e., similar to the measured OH profile in Figure 7) and does not show the hump feature that appears in the constant $U-V$ model in Figure 7. Thus, the departure from the constant $U-V$ reactor model was not caused by using the driver insert.

4.2. Higher Temperature (1200 K < T < 1460 K) Example Case. As temperature rises above 1200 K, H_2O formation starts to show increasingly pronounced sensitivity to the reaction $OH + H_2O_2 \rightarrow H_2O + HO_2$, as can be seen from Figure 9 at 1398 K. The apparent reason is that H_2O_2 is mainly consumed by its thermal decomposition at lower temperatures ($1000 < T < 1200$ K). However, at elevated temperatures, OH concentration increases dramatically such that the reaction $OH + H_2O_2 \rightarrow H_2O + HO_2$ becomes an important channel in the removal of H_2O_2. Radical−radical reactions that lead to final products (H_2O and O_2) are typically very fast, and the consumption of H_2O_2 is the rate-limiting step, either through $H_2O_2 + M \rightarrow 2OH + M$ or $OH + H_2O_2 \rightarrow H_2O + HO_2$. Therefore, at elevated temperatures, k_1 could not be solely determined from H_2O concentration time-histories.

Fortunately, the OH sensitivity coefficient plot in Figure 10 shows that both the reaction rates (k_1 and k_2) that control H_2O formation also control OH yields. With two constraints (H_2O and OH), it is possible to determine two independent unknowns (k_1 and k_2). In addition, the problem is well posed because k_1 and k_2 sensitivities to H_2O are similar, whereas the OH sensitivities have opposite signs. In the current study, H_2O and OH time-histories of all the tests performed at higher temperatures ($1200 < T < 1460$ K) were analyzed at the same time to infer both k_1 and k_2 with small uncertainties.

Example H_2O and OH profiles of the test conditions of Figure 9 are presented in Figures 11 and 12, respectively. We used a search algorithm to evaluate k_1 and k_2. Specifically, the best-fit k_1 and k_2 were determined iteratively between the profiles of the two species, beginning by adjusting k_1 and k_2 together to match H_2O time-histories with k_1/k_2 ratios fixed at the values estimated from $[OH]_{peak}$. k_2 values were then fine-tuned to match OH time-histories while keeping k_1 unchanged to get updated k_1/k_2 ratios. The process continued until good fits had been achieved for both species time-histories. The sensitivity coefficient plots in Figures 9 and 10 were generated using GRI-Mech[16] with experimentally evaluated k_1 and k_2.

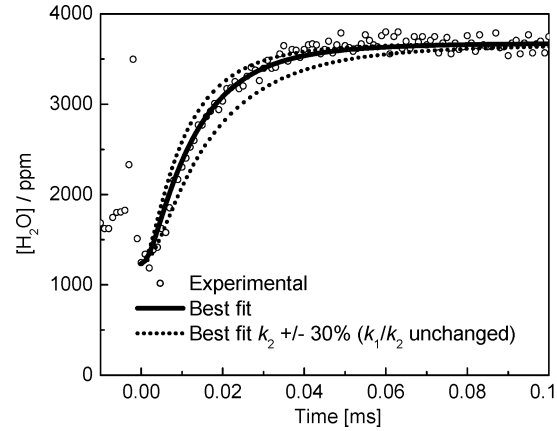

Figure 11. H_2O time-history recorded at the conditions of Figure 9. The best-fit H_2O profile was achieved by setting $k_1 = 2.4 \times 10^9$ [cm^3 mol^{-1} s^{-1}] and $k_2 = 6.8 \times 10^{12}$ [cm^3 mol^{-1} s^{-1}]. In comparison, the calculated curves with both k_1 and k_2 changed ±30% while keeping k_1/k_2 as determined from the corresponding OH profile.

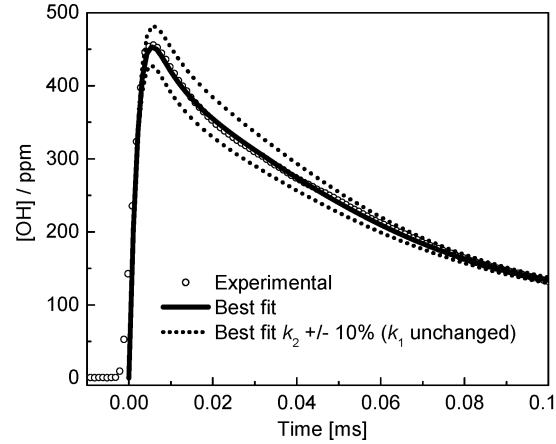

Figure 12. OH time-history recorded at the conditions of Figure 9. The best-fit OH profile was achieved by the same pair of k_1 and k_2 values that best-fits the water profile in Figure 11. The calculated curves with k_2 changed ±10% while keeping k_1 at its overall optimal value.

Besides the search algorithm, other optimization methods[34,37,38] have been developed to simultaneously analyze a variety of experimental data, including ignition delay times, flame speeds, and species time-histories. These experimental data are the target constraints of combustion mechanisms, although the data usually contain similar and redundant information about the systems. Typically, the optimal solution for one set of data is not the optimal solution for another set of data, due to experimental errors. Fortunately, the current search algorithm is suitable for a low-dimensionality system.[34] Of the H_2O_2 thermal decomposition system under investigation, there are only two major active parameters (k_1 and k_2). Furthermore, the two active parameters have well-behaved *and different* functional influence on the time-histories of OH and H_2O obtained from individual experiments, thus permitting a unique determination of both reaction rate constants.

Recall that at lower temperatures ($1000 < T < 1200$ K), the initial H_2O_2 loading was determined by taking the difference between the initial and the final plateau H_2O levels without corrections.[21] The accuracy of the approach is satisfactory at lower temperatures since near-complete (>99%) conversions to final products (H_2O and O_2) following the decomposition of H_2O_2 can be assumed. Chemical kinetics calculations show that H_2O_2 and HO_2 are depleted when a H_2O plateau is reached. A small fraction of the initial H_2O_2 is converted to and remains as OH, but this represents typically less than 0.5% of the initial water concentration.

At high temperatures, initial H_2O_2 concentration must be related to both the final H_2O and OH concentrations. For the example case at 1398 K, there is a residual OH concentration of approximately 130 ppm at 0.1 ms (Figure 12) when the apparent H_2O plateau was achieved (Figure 11). The initial H_2O_2 concentration must thus be increased by 65 ppm to correct for the residual OH. Similar adjustments were made for all the tests conducted at temperatures higher than 1200 K. Good agreement was found between chemical kinetics calculations using corrected H_2O_2 initial concentrations and experimental observations.

k_1 and k_2 errors stem from uncertainties in fitting, uncertainty in temperature, and uncertainties in interfering reactions. The fitting uncertainties of k_1 and k_2 were estimated jointly. By setting a constant k_1/k_2 ratio, k_1 and k_2 can both be determined within ±15% accuracy by fitting the H_2O profile, as illustrated in Figure 11. In addition, the k_1/k_2 ratio has an estimated fitting error of ±4% as derived from the OH profile (Figure 12). The overall fitting uncertainty for both k_1 and k_2 are bounded by ±16%, which is the root-sum-square (RSS) of the two separate fitting uncertainties. The uncertainty in k_1 associated with temperature uncertainty was estimated to be ±21%.[21] By contrast, the uncertainties in k_2 resulting from temperature uncertainty and OH absorption cross-section uncertainty were evaluated to be ±2 and ±5% as discussed in Section 4.1 of the current study. Uncertainty from interfering reactions was estimated to be less than ±3% for both k_1 and k_2. Therefore, the overall uncertainties for k_1 and k_2 are less than ±27% and ±17%, respectively, for the example case at $T = 1398$ K.

We also found that the difference between OH profiles calculated using the constant $U-V$ and the constant $P-H$ reactor models diminishes as temperature increases. The trend coincides with our expectation, because the decomposition of H_2O_2 is greatly enhanced at elevated temperatures and the OH formation rate via H_2O_2 thermal decomposition becomes comparable to the OH removal rate via the reaction $OH + H_2O_2 \rightarrow H_2O + HO_2$. As the temperature-sensitive H_2O_2 decomposition reaction losses its dominance in the H_2O_2 decomposition system, OH profiles show less sensitivity to temperatures. This observation may in turn justify the constant $P-H$ reactor model we adopted to address the discrepancies between experimentally observed OH profiles and calculations based on the constant $U-V$ reactor model.

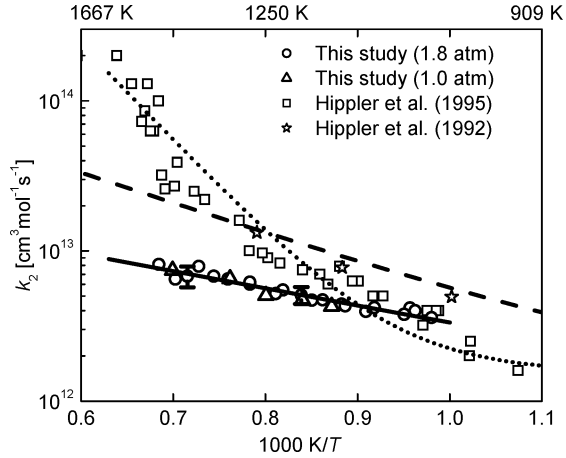

Figure 13. Arrhenius plot of the rate of the reaction $OH + H_2O_2 \rightarrow H_2O + HO_2$ (k_2). The solid line is the linear-fit to all the experimental data of the current study. The dashed line is the rate expression used by Ó Conaire et al.[17] and Li et al.,[18] whereas the dotted line is the one adopted by GRI-Mech.[16]

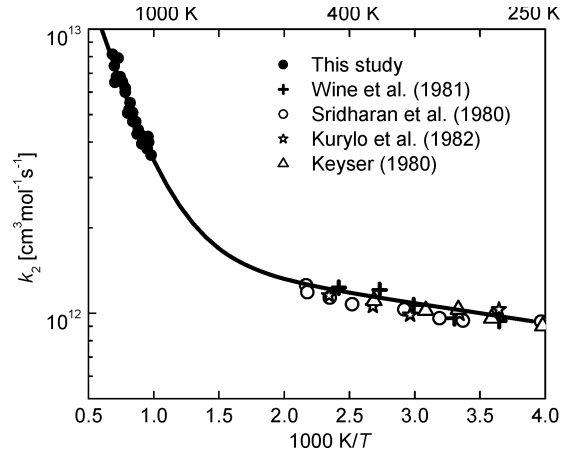

Figure 14. The reaction rate of $OH + H_2O_2 \rightarrow H_2O + HO_2$ (k_2), displays a non-Arrhenius behavior over a wide temperature range. Experimental data are well-represented by a sum of two Arrhenius expressions (solid line).

4.3. Arrhenius Plot of the Reaction $OH + H_2O_2 \rightarrow H_2O + HO_2$. Using the approaches described in Sections 4.1 and 4.2, the rate constant of reaction 2, $OH + H_2O_2 \rightarrow H_2O + HO_2$, was determined at 1.8 atm over the entire temperature range from 1000 to 1460 K. Experimental data were plotted in an Arrhenius plot in Figure 13 ,and are compared to the results reported by Hippler et al.[13,14] The current study shows reasonable agreement with the previous studies at lower temperatures ($T <$ 1300 K). However, at temperatures higher than 1300 K, the study by Hippler et al.[14] reported a dramatic increase in the reaction rate. Since the measurements made by Hippler et al.[13,14] were the only available experimental data, their values were widely used in combustion mechanisms,[16−19] as represented by the dotted line and the dashed line in Figure 13.

We also carried out rate measurements at 1 atm. As the total pressure decreased from 1.8 to 1 atm, the OH formation rate is reduced almost by half, since the major OH formation channel $H_2O_2 + M \rightarrow 2OH + M$ is pressure dependent, whereas the

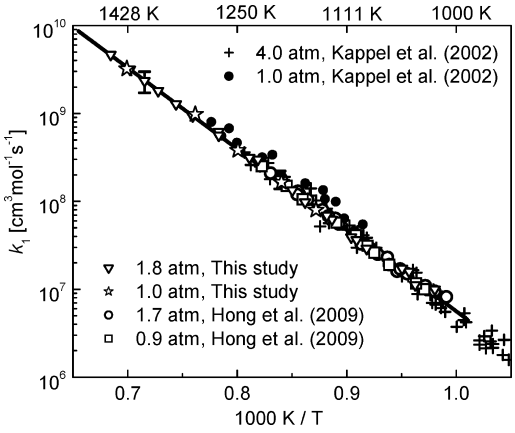

Figure 15. Arrhenius plot of the second-order rate coefficient for H_2O_2 thermal decomposition (k_1). Excellent agreement was found between the current study and previous studies.[15,21] The solid line is the linear-fit to the experimental data of this study at 1.8 atm (bath gas: argon).

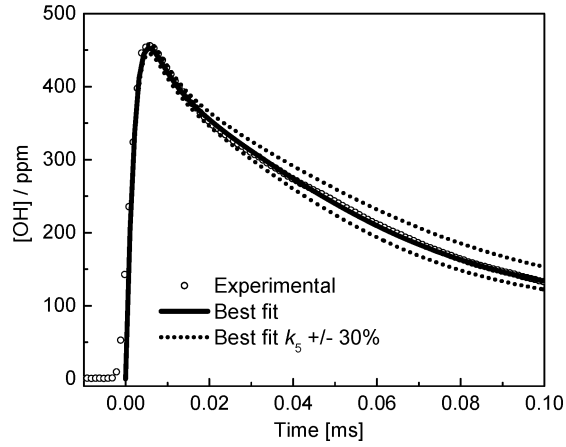

Figure 16. OH time-history recorded at the conditions of Figure 9. The optimal rate of the reaction $2OH \rightarrow H_2O + O$ (k_5) was determined by best-fitting the OH time-history. The calculated curves with k_5 changed ±30% while retaining the values of all other parameters.

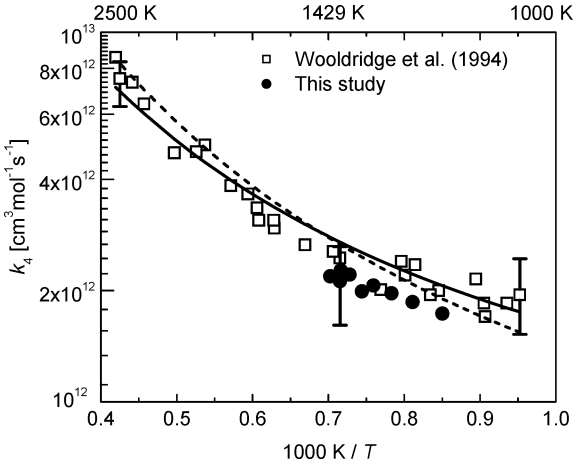

Figure 17. Arrhenius plot of the secondary reaction $2OH \rightarrow H_2O + O$ (k_5). The results obtained in the current study are within the estimated error bars of Wooldridge et al.[35] The solid line is the rate expression used by Wooldridge et al.[35] The dashed line is the rate expression reported by Michael[42] corrected for the updated OH heat of formation.

OH removal channel $OH + H_2O_2 \rightarrow H_2O + HO_2$ is not.[14,39] Measured OH yields at 1 atm were expected to be approximately half of those at 1.8 atm to recover a pressure-independent k_2. As demonstrated in Figure 13, the data obtained from 1 and 1.8 atm experiments show remarkable consistency, suggesting a low likelihood for systematic error. A linear fit to all the data (1 and 1.8 atm) yields an expression

$$k_2 = 10^{13.66}\exp(-2630\ \mathrm{K}/T)\ [\mathrm{cm^3\ mol^{-1}\ s^{-1}}] \quad (1020 < T < 1460\ \mathrm{K})$$

We performed a simple Arrhenius fit to all of the Hippler et al. data[14] to yield an A-coefficient of 4.6×10^{16} [cm^3 mol^{-1} s^{-1}] and an activation energy of 19.7 kcal/mol. The ab initio calculations by Ginovska et al.[39] reveal that the barrier heights on the ground state pathways is only 7.3 or 7.8 kcal/mol[39] above the precursor complex (H_3O_3), whereas the precursor complex is 6.2 kcal/mol lower in energy than the separated H_2O_2 and OH species. The activation energy from this study is 5.2 kcal/mol, which is in better agreement with the theoretical calculations. As well, the effective A-coefficient from Hippler et al.[14] is unusually large. By comparison, the A-coefficient resulting from the current study, 4.6×10^{13} [cm^3 mol^{-1} s^{-1}], is a more reasonable value.

To account for the discrepancy between the current study and that of Hippler et al.,[14] experimental procedures of the previous study were carefully reviewed. The thermal decomposition rate of H_2O_2 (k_1) utilized in their study was approximately 40% larger than determined in the current study, which translated to an approximate 40% difference in k_2. Their first example (Figure 1 of ref 14, $T = 1152$ K) yields a new $k_2 = 4.2$ [cm^3 mol^{-1} s^{-1}], in good agreement with our current study, if their data are reevaluated with our H_2O_2 thermal decomposition rate.

However, at elevated temperatures, the large discrepancy in k_2 (more than a factor of 3) cannot be explained by utilizing different values for k_1. Unfortunately, absolute OH yields for a high temperature example case (Figure 3 of ref 14, $T = 1566$ K) were not provided. However, by examining the experimental conditions included in the paper (Table 3 of ref 14), we found a dramatic decrease in [H_2O_2] of the test mixtures, dropping from 1220 ppm at 931 K to 54 ppm at 1678 K. Given that a sensitive H_2O_2 diagnostic was not available when the work[14] was accomplished, they had to derive [H_2O_2] from the early rises in OH time-histories and the thermal decomposition rate of H_2O_2 determined in separate studies.[40,41] Without providing an explanation for such dramatic reduction in [H_2O_2], we conjecture that the measured OH yields were only fractions of the true values. This may in turn explain their rate of the OH removal reaction $OH + H_2O_2 \rightarrow H_2O + HO_2$ (k_2) being too large at high temperatures. We also noticed that Hippler et al.[14] conducted their experiments at pressures near 0.4 atm. The OH absorption feature is narrow at those low pressures as the pressure broadening[22] is less pronounced, resulting in a higher uncertainty in OH absorption cross-section.

Most previous studies of k_2 were carried out near room temperature. The studies by Wine,[2] Sridharan,[8] Kurylo,[4] and Keyser[5] show remarkable consistency and are plotted in Figure 14 along with the results of this study (both at 1 and 1.8 atm). A strong non-Arrhenius behavior is apparent. All the experimental data can be well represented by a sum of two Arrhenius expressions:

$$k_2 = 10^{12.24}\exp(-160\ \mathrm{K}/T) + 10^{13.88}\exp(-3660\ \mathrm{K}/T)\ [\mathrm{cm^3\ mol^{-1}\ s^{-1}}] \quad (280 < T < 1640\ \mathrm{K})$$

TABLE 1: Test Conditions and Results of H_2O_2 Decomposition Experiments in Argon Bath Gas[a]

T (K)	P (atm)	[H_2O] (ppm)	[H_2O_2] b (ppm)	k_1 (M = Ar) (cm^3 mol^{-1} s^{-1})	k_2 (cm^3 mol^{-1} s^{-1})	k_5 (cm^3 mol^{-1} s^{-1})
1221	1.921	1793	2827	3.0×10^8	5.5×10^{12}	
1192	1.949	1364	2216	1.8×10^8	5.1×10^{12}	
1160	2.008	480	1500	9.8×10^7	4.7×10^{12}	
1133	2.070	842	1291	6.4×10^7	4.4×10^{12}	
1106	2.126	1043	378	3.9×10^7	4.0×10^{12}	
1045	2.066	1235	1670	1.6×10^7	4.2×10^{12}	
1039	2.192	2196	3632	1.1×10^7	4.0×10^{12}	
1020	2.192	1218	3360	1.0×10^7	3.6×10^{12}	
1089	2.239	725	1678	2.9×10^7	4.2×10^{12}	
1277	2.031	324	2200	6.2×10^8	6.0×10^{12}	
1052	1.966	826	2204	1.7×10^7	3.8×10^{12}	
1100	1.947	1538	2444	3.6×10^7	4.0×10^{12}	
1128	1.884	1042	3210	6.2×10^7	4.3×10^{12}	
1176	1.810	988	3256	1.3×10^8	4.7×10^{12}	1.7×10^{12}
1233	1.746	514	2228	3.1×10^8	5.2×10^{12}	1.9×10^{12}
1344	1.974	608	2836	1.3×10^9	6.8×10^{12}	2.0×10^{12}
1277	2.020	1038	3011	5.6×10^8	6.2×10^{12}	2.0×10^{12}
1317	2.011	1166	2729	9.3×10^8	6.5×10^{12}	2.1×10^{12}
1374	1.945	1062	2684	1.8×10^9	7.9×10^{12}	2.2×10^{12}
1398	1.909	1234	2540	2.4×10^9	6.8×10^{12}	2.3×10^{12}
1424	1.868	1357	3148	3.0×10^9	6.5×10^{12}	2.2×10^{12}
1461	1.834	1346	2837	4.7×10^9	8.2×10^{12}	
1134	1.874	816	2900	6.9×10^7	4.5×10^{12}	
1430	1.039	1154	3367	3.2×10^9	7.4×10^{12}	
1313	1.057	1170	3250	9.7×10^8	6.5×10^{12}	
1249	1.113	1218	3806	3.8×10^8	5.1×10^{12}	
1190	1.152	786	3650	1.7×10^8	4.7×10^{12}	
1147	1.224	775	3157	8.0×10^7	4.3×10^{12}	

[a] The H_2O_2 and H_2O concentrations are initial values.

4.4. Arrhenius Plot of the Reaction $H_2O_2 + M \rightarrow 2OH + M$. By combining the H_2O and OH diagnostics, the measurements of H_2O_2 decomposition rate have been extended beyond the higher limit of the temperature range of our previous study (1200 K) to 1460 K.[21] Results of this study and previous studies[15,21] are shown in Figure 15.

Excellent agreement was found between the current study and the previous study[21] over the entire overlapped temperature range from 1000 to 1200 K. It was also confirmed that the pressure dependence of k_1 is negligible at pressures lower than 2 atm, as reported in the previous study. The linear-fit to the data obtained at 1.8 atm of this study thus yields a determination of the low-pressure limit of H_2O_2 decomposition rate in argon:

$$k_1 = 10^{15.98} \exp(-21250\ \mathrm{K}/T)\ [\mathrm{cm^3\ mol^{-1}\ s^{-1}}] \quad (1020 < T < 1460\ \mathrm{K})$$

By comparison, the low-pressure limit in argon obtained in the previous study[21] can be represented by the expression $k_1 = 10^{15.97} \exp(-21\,220\ \mathrm{K}/T)$ [cm^3 mol^{-1} s^{-1}] for temperatures between 1000 and 1200 K, showing extraordinary consistency.

4.5. Secondary Reaction $2OH \rightarrow H_2O + O$. The OH sensitivity coefficient plot for the example case at the elevated temperature (Figure 10) reveals that the reaction $2OH \rightarrow H_2O + O$ becomes an important OH removal channel after the OH peak. The rates of the two other reactions that show substantial sensitivities during the OH decay, $H_2O_2 + M \rightarrow 2OH + M$ and $OH + H_2O_2 \rightarrow H_2O + HO_2$, have been determined relatively accurately in the present study. Therefore, a good estimation can be obtained for the rate of the secondary reaction $2OH \rightarrow H_2O + O$ (k_5) by varying its value in the chemical kinetics mechanism to capture the trend of OH decay. For the example case at 1398 K of this study, the best-fit OH profile is presented in Figure 16, in comparison with the ones calculated with k_5 values 30% above or below its optimal value.

Recalling the discussion earlier in the paper (Section 4.1) regarding the difference between using a constant $U-V$ and a constant $P-H$ model, the question arises, are the k_5 values inferred from the decay of OH susceptible to the choice of these two models. The issue is found to be minor by a careful examination of Figures 5 and 7, because the predictions by the two models converge when the reaction $2OH \rightarrow H_2O + O$ becomes an important OH removal channel.

Major error sources of k_5 include uncertainty in fitting, uncertainties in k_1 and k_2, and uncertainty in temperature. The fitting uncertainty was estimated to be ±15%. Following the discussion in Section 4.1, the temperature uncertainty in k_1 and k_2 does not propagate to k_5. The uncertainty inherited from k_1 and k_2 is mainly from their fitting errors (±16%, see Section 4.2) and was evaluated to be ±17% by varying k_5 to best-fit the OH time-history while k_1 and k_2 were at the limits of their fitting uncertainties. The uncertainty in k_5 associated with temperature uncertainty was estimated to be ±5%. Therefore, the overall uncertainty of k_5 is ±24%.

Similar best-fit procedures were carried out for the tests at temperatures higher than 1176 K. For the tests conducted at temperatures lower than 1176 K, OH yields were so low that $2OH \rightarrow H_2O + O$ is a minor channel for OH decay. All of the inferred k_5 values are plotted in Figure 17. k_5 has been measured by Wooldridge et al.[35] with estimated uncertainties of −16% to +11% at $T > 2100$ K and −22% to +25% at $T = 1050$ K. The k_5 values determined in the present study are in good agreement with those of the Wooldridge et al.[35]

In addition, the reverse reaction $O + H_2O \rightarrow 2OH$ has been experimentally investigated[36,43] and an expression for k_5 has been derived from these two studies using equilibrium constants.[42] Correcting for the updated OH heat of formation,[22,30] k_5 is well

represented by $4.34 \times 10^3\ T^{2.7} \exp(951/T)$ [cm^3 mol^{-1} s^{-1}], in good agreement with the expression $k_5 = 3.57 \times 10^4\ T^{2.40} \exp(1063/T)$ [cm^3 mol^{-1} s^{-1}] recommended by Wooldridge et al.[35]

5. Conclusions

The H_2O_2 thermal decomposition system was studied behind reflected shock waves over the temperature range between 1020 and 1460 K using laser absorption diagnostics for both H_2O and OH. Good detectivity for H_2O was achieved using tunable diode laser absorption of water at 2550.96 nm within its υ_3 fundamental band. The initial compositions of the reactant mixtures were determined using the sensitive H_2O diagnostic. OH absorption was measured using the well-characterized $R_1(5)$ line of the OH $A^2\Sigma^+ - X^2\Pi$ (0,0) band near 306.7 nm.

The determinations of the thermal decomposition rate of H_2O_2 (k_1) were extended to 1460 K by jointly interpreting H_2O and OH time-histories. The low-pressure reaction rate was found to be $k_1 = 10^{15.98} \exp(-21\ 250\ \text{K}/T)$ [cm^3 mol^{-1} s^{-1}], in excellent agreement with the previous study.[21] The estimated uncertainties of k_1 were $\pm 27\%$ for temperatures higher than 1200 K and $\pm 23\%$ for temperatures between 1000 and 1200 K.

The rate of the reaction $OH + H_2O_2 \rightarrow H_2O + HO_2$ (k_2) was evaluated at pressures of 1 and 2 atm, over the entire temperature range between 1020 and 1460 K by analyzing the time-histories of H_2O and OH. No pressure dependence of the reaction rate was found. The measurements can be represented by the Arrhenius expression $k_2 = 10^{13.66} \exp(-2630\ \text{K}/T)$ [cm^3 mol^{-1} s^{-1}] over the measured temperature range with an overall uncertainty ranging from $\pm 13\%$ at low temperatures to $\pm 17\%$ at high temperatures. Non-Arrhenius behavior was found by comparing the results of the current study to the previous measurements near room temperature.[2,4,5,8] Over a wide temperature range from 280 to 1640 K, the behavior can be described by a sum of two Arrhenius expressions: $k_2 = 10^{12.24} \exp(-160\ \text{K}/T) + 10^{13.88} \exp(-3660\ \text{K}/T)$ [cm^3 mol^{-1} s^{-1}].

The rate of a secondary reaction $2OH \rightarrow H_2O + O$ (k_5) was evaluated by examining the decay of OH at elevated temperatures ($T > 1176$ K). The results were well within the estimated uncertainty limits of the work of Wooldridge et al.[35] Their rate expression $k_5 = 10^{4.55} T^{2.40} \exp(1063\ \text{K}/T)$ [cm^3 mol^{-1} s^{-1}] ($298 < 2380$ K) is supported by the present study.

Appendix

Acknowledgment. This work was primarily supported by the National Science Foundation under award No. 0649936 with partial support from the Department of Energy, Office of Basic Energy Sciences, with Dr. Wade Sisk as technical monitor, and the Department of Energy [National Nuclear Security Administration] under Award No. NA28614. The authors are grateful to their associates at Stanford University, Professor David M. Golden for helpful discussions, and Shengkai Wang for technical support.

References and Notes

(1) Westbrook, C. *Proc. Combust. Institute* **2000**, *28*, 1563–1577.
(2) Wine, P. H.; Semmes, D. H.; Ravishankara, A. R. *J. Chem. Phys.* **1981**, *75*, 4390–4395.
(3) Vaghjiani, G. L.; Ravishankara, A. R.; Cohen, N. *J. Chem. Phys.* **1989**, *93*, 7833–7837.
(4) Kurylo, M.; Murphy, J. L.; Haller, G. S.; Cornett, K. D. *Int. J. Chem. Kin.* **1982**, *14*, 1149–1161.
(5) Keyser, L. F. *J. Phys. Chem.* **1980**, *84*, 1659–1663.
(6) Jiménez, E.; Gierczak, T.; Stark, H.; Burkholder, J. B.; Ravishankara., A. R. *J. Phys. Chem. A* **2004**, *108*, 1139–1149.
(7) Lamb, J. J.; Molina, L. T.; Smith, C. A.; Molina, M. J. *J. Phys. Chem.* **1980**, *87*, 4467–4470.
(8) Sridharan, U. C.; Reimann, B.; Kaufman, F. *J. Chem. Phys.* **1980**, *73*, 1286–1293.
(9) Vakhtin, A. B.; McCabe, D. C.; Ravishankara, A. R.; Leone, S. R. *J. Phys. Chem. A* **2003**, *107*, 10642–10647.
(10) Mellouki, A.; Teton, S.; Laverdet, G.; Quilgars, A.; Le Bras, G. *J. Chim. Phys.* **1994**, *91*, 473–487.
(11) Sander, S. P. ; Friedl, R. R. ; Ravishankara, A. R. ; Golden, D. M. ; Kolb, C. E. ; Kurylo, M. J. ; Molina, M. J. ; Moortgat, G. K.; Finlayson-Pitts, B. J. ; Wine, P. H. ; Huie, R. E. ; Orkin, V. L. *Chemical Kinetics and Photochemical Data for Use in Atmospheric Studies Evaluation Number 15*; Jet Propulsion Laboratory, California Institute of Technology: Pasadena, CA, 2006. http://jpldataeval.jpl.nasa.gov/ (accessed September 24, 2009).
(12) Atkinson, R.; Baulch, D. L.; Cox, R. A.; Crowley, J. N.; Hampson, R. F.; Hynes, R. G.; Jenkin, M. E.; Rossi, M. J.; Troe, J. *Atmos. Chem. Phys.* **2004**, *4*, 1461–1738.
(13) Hippler, H.; Troe, J. *Chem. Phys. Lett.* **1992**, *192*, 333–337.
(14) Hippler, H.; Neunaber, H.; Troe, J. *J. Chem. Phys.* **1995**, *103*, 3510–3516.
(15) Kappel, Ch.; Luther, K.; Troe, J. *Phys. Chem. Chem. Phys.* **2002**, *4*, 4392–4398.
(16) Smith, G. P.; Golden, D. M.; Frenklach, M.; Moriarty, N. W.; Eiteneer, B.; Goldenberg, M.; Bowman, C. T.; Hanson, R. K.; Song, S.; Gardiner, W. C.; Lissianski, V. V.; Qin, Z. GRI-Mech 3.0. http://www.me.berkeley.edu/grimech/ (accessed March 12, 2009).
(17) Ó Conaire, M.; Curran, H. J.; Simmie, J. M.; Pitz, W. J.; Westbrook, C. K. *Intl. J. Chem. Kinet.* **2004**, *36*, 603–622.
(18) Li, J.; Zhao, Z.; Kazakov, A.; Dryer, F. L. *Intl. J. Chem. Kinet.* **2004**, *36*, 566–575.
(19) Konnov, A. A. *Combust. Flame* **2008**, *152*, 507–528.
(20) Baulch, D. L.; Bowman, C. T.; Cobos, C. J.; Cox, R. A.; Just, Th.; Kerr, J. A.; Pilling, M. J.; Stocker, D.; Troe, J.; Tsang, W.; Walker, R. W.; Warnatz, J. *J. Phys. Chem. Ref. Data* **2005**, *34*, 757–1397.
(21) Hong, Z.; Farooq, A.; Barbour, E. A.; Davidson, D. F.; Hanson, R. K. *J. Phys. Chem. A* **2009**, *113*, 12919–12925.
(22) Herbon, J. T.; Hanson, R. K.; Golden, D. M.; Bowman, C. T. *Proc. Combust. Institute* **2002**, *29*, 1201–1208.
(23) Hong, Z.; Pang, G. A.; Vasu, S. S.; Davidson, D. F.; Hanson, R. K. *Shock Waves* **2009**, *19*, 113–123.
(24) Farooq, A.; Jeffries, J. B.; Hanson, R. K. *Appl. Phys. B: Laser Opt.* **2009**, *96*, 161–173.
(25) Goldman, A.; Gamache, R. R.; Perrin, A.; Flaud, J. M.; Rinsland, C. P.; Rothman, L. S. *J. Quant. Spectrosc. Radiat. Transfer* **2000**, *66*, 455–486.
(26) Vasudevan, V.; Davidson, D. F.; Hanson, R. K. *J. Phys. Chem. A* **2005**, *109*, 3352–3359.
(27) Davidson, D. F.; Oehlschlaeger, M. A.; Herbon, J. T.; Hanson, R. K. *Proc. Combust. Institute* **2002**, *29*, 1295–1301.
(28) Ludwig, W.; Brandt, B.; Friedrichs, G.; Temps, F. *J. Phys. Chem. A* **2006**, *110*, 3330–3337.
(29) Lutz, A. E.; Kee, R. J.; Miller, J. A. *Senkin: A FORTRAN Program for Predicting Homogeneous Gas Phase Chemical Kinetics with Sensitivity Analysis*, Report No. SAND87−8248; Sandia National Laboratory: Albuquerque, NM, 1988.
(30) Ruscic, B.; Wagner, A. F.; Harding, L. B.; Asher, R. L.; Feller, D.; Dixon, D. A.; Peterson, K. A.; Song, Y.; Qian, X. M.; Ng, C. Y.; Liu, J. B.; Chen, W. W. *J. Phys. Chem. A* **2002**, *106*, 2727–2747.
(31) Ruscic, B.; Pinzon, R. E.; Morton, M. E.; Srinivasan, N. K.; Su, M.-C.; Sutherland, J. W.; Michael, J. V. *J. Phys. Chem. A* **2006**, *110*, 6592–6601.
(32) Hong, Z.; Vasu, S. S.; Davidson, D. F.; Hanson, R. K. *J. Phys. Chem. A* **2010**, DOI: 10.1021/jp100739t.
(33) Box, G.; Meyer, R. D. *J. Res. Nat. Bur. Stand.* **1985**, *90*, 495–500.
(34) Frenklach, M.; Wang, H.; Rabinowitz, M. J. *Prog. Energy Combust. Sci.* **1992**, *18*, 47–73.
(35) Wooldridge, M. S.; Hanson, R. K.; Bowman, C. T. *Int. J. Chem. Kin.* **1994**, *26*, 389–401.
(36) Sutherland, J. W.; Patterson, P. M.; Klemm, R. B. *Symp. (Intl.) Combust.* **1991**, *23*, 51–57.
(37) Harris, S. D.; Elliott, L.; Ingham, D. B.; Pourkashanian, M.; Wilson, C. W. *Comput. Methods Appl. Mech. Engrg.* **2000**, *190*, 1065–1090.
(38) Qin, Z.; Lissianski, V. V.; Yang, H.; Gardiner, W. C.; Davis, S. G.; Wang, H. *Proc. Combust. Inst.* **2000**, *28*, 1663–1669.
(39) Ginovska, B.; Camaioni, D. M.; Dupuis, M. *J. Chem. Phys.* **2007**, *127*, 084309.
(40) Troe, J. *Ber. Bunsen-Ges.* **1969**, *73*, 946–952.
(41) Kijewski, H.; Troe, J. *Helv. Chim. Acta* **1972**, *55*, 205–213.
(42) Michael, C. V. *Prog. Energy Combust. Sci.* **1992**, *18*, 327–347.
(43) Lifshitz, A.; Michael, J. V. *Symp. (Intl.) Combust.* **1991**, *23*, 59–67.

JP100204Z